Structure of Barite (001)− and (210)−Water Interfaces

P. Fenter,*,† M. T. McBride,‡ G. Srajer,§ N. C. Sturchio,†,∥ and D. Bosbach⊥

Environmental Research Division, Argonne National Laboratory, Argonne, Illinois 60439-4843, Chemistry and Materials Science Division, Lawrence Livermore National Laboratory, 7000 East Avenue, L-350, Livermore, California 94551, Experimental Facilities Division, Advanced Photon Source, Argonne National Laboratory, Argonne, Illinois 60439, Department of Earth and Environmental Sciences, University of Illinois at Chicago, 845 West Taylor Street (MC-186), Chicago, Illinois 60607, and Forschungszentrum Karlsruhe, Institut für Nukleare Entsorgung, Postfach 3640, 76021 Karlsruhe, Germany

The structures of the barite (001) and (210) cleavage surfaces were measured in contact with deionized water at 25 °C. High resolution (∼1 Å) specular X-ray reflectivity and atomic force microscopy were used to probe the step structures of the cleaved surfaces and the atomic structures of the barite–water interfaces including the structures of water near the barite–water interfaces. The barite (001) and (210) cleavage surfaces are characterized by large (>2500 Å) domains separated by unit-cell steps (7.15 and 3.44 Å steps for the (001) and (210) surfaces, respectively). This observation was unanticipated for the (001) surface in which adjacent $BaSO_4$ layers are displaced vertically by $c/2$ and symmetry related through a 2_1 screw axis along (001). The atomic structures of the two cleavage surfaces derived by X-ray reflectivity reveal that near-surface sulfate groups exhibit significant (∼0.4 Å) structural displacements, while Ba surface ion displacements are significantly smaller (∼0.07 Å). Water adsorbs to the barite surfaces in a manner consistent, in both number and height, with the saturation of broken Ba–O bonds; no evidence was found for additional structuring of the fluid water near the surface.

1. Introduction

The barite–water interface has been studied intensely because of the problem of barite scale formation in the petroleum industry.[1] Barite precipitates when sulfate-rich seawater reacts with Ba-rich sedimentary formation waters, forming scale deposits that restrict flow in pipes used for petroleum production. Because barite scale formation can be impeded by the addition of growth inhibitors, most relevant studies to date have concentrated on understanding the mechanisms of barite crystal growth in the presence and absence of growth inhibitors.[2–5] Other studies have explored the possibility of enhancing the barite dissolution rate with chelating agents.[6,7]

The (001) and (210) surfaces are the dominant barite surfaces expressed under most experimental conditions, both for natural and synthetic crystals.[8–10] Consequently, an understanding of these two surface orientations provides direct insight into the properties of barite under a wide range of conditions. There are, however, a number of fundamental issues that have yet to be resolved, even for these two well-defined barite–water interfaces. At moderate to high supersaturation, barite grows by island nucleation on flat terraces,[2,3] yet relatively little is known about the structure of this nucleation site, i.e., the terrace

areas at the barite–water interface. Atomic force microscopy (AFM) studies of the (001) surface at molecular resolution have shown that the surface unit mesh is a (1 × 1) symmetry, with an apparent corrugation of ∼1.3 Å that is in general agreement with the bulk crystal structure.[2] Molecular modeling (using predefined force fields) of the barite–vacuum interface predicted that the (001) and (210) surfaces are the most stable surfaces.[11] The energetic changes due to surface relaxation of these facets were found to be small, but the magnitude and direction of these molecular displacements were not specified, and interaction of water with these surfaces was not included in the calculation. These conclusions have yet to be directly tested.

The barite–water interface is a system in which the structure of interfacial water might be probed directly. To date, relatively few mineral–water interfaces have been characterized by high-resolution structural measurements.[12–17] Other comparable studies have been of electrode–electrolyte interfaces under potentiometric control.[18–20] Thus we can begin to compare trends in the near-surface water structures among these different systems.

We characterized the (001) and (210) barite–water interface structures (Figure 1) using high-resolution specular X-ray reflectivity and atomic force microscopy. These measurements have elucidated the defect structures of freshly cleaved surfaces, structural relaxations at the barite–water interface as a function of depth, and the termination of bonds broken by cleavage.

2. Experimental Details

X-ray Reflectivity. X-ray scattering is an ideal technique for probing mineral–fluid interface structure because X-rays penetrate macroscopic quantities of fluids (such as water) with limited attenuation. The interaction of X-rays with matter is well understood from a fundamental perspective, yielding a direct

* Author to whom correspondence should be addressed at Argonne National Laboratory, ER-203, 9700 S. Cass Ave., Argonne, IL 60439. Fax: 630-252-7415. E-mail: fenter@anl.gov.
† Environmental Research Division, Argonne National Laboratory.
‡ Chemistry and Materials Science Division, Lawrence Livermore National Laboratory.
§ Experimental Facilities Division, Advanced Photon Source, Argonne National Laboratory.
∥ Department of Earth and Environmental Sciences, University of Illinois at Chicago.
⊥ Forschungszentrum Karlsruhe, Institut für Nukleare Entsorgung.

Structure of Barite (001)− and (210)−Water Interfaces

J. Phys. Chem. B, Vol. 105, No. 34, 2001 **8113**
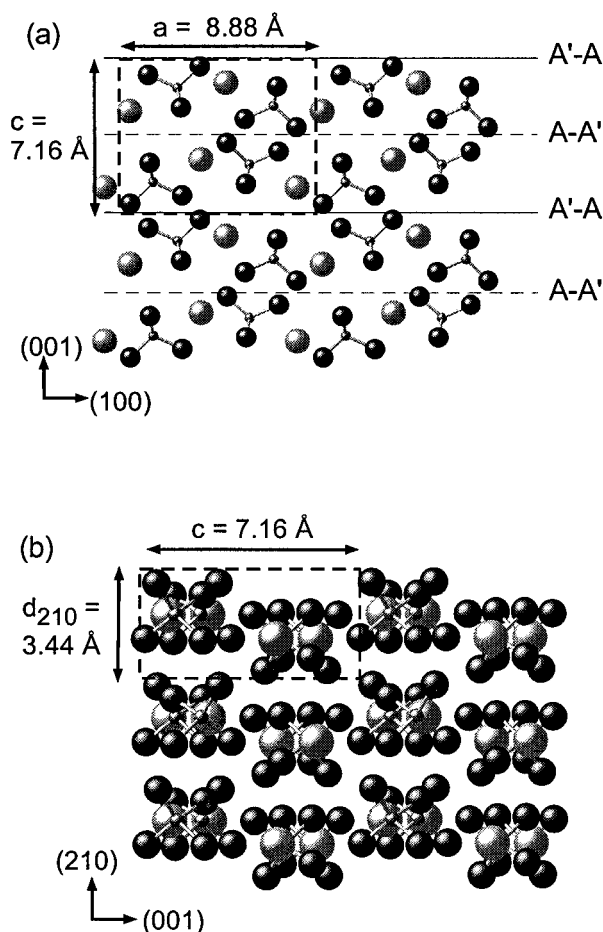
Figure 1. Perspective view of the (001) and (210) barite crystal structures, respectively, showing the Ba atoms as large light circles, S atoms as small light circles, and O atoms as large dark circles. Crystallographic directions are noted in each. In (a), alternating A−A′ and A′−A cleavage planes are indicated. The outermost sulfate groups are tilted in opposite directions for these two cleavage planes due to the presence of a screw axis along [001].

relation between the interface *structure* and the scattering intensity. The X-ray reflectivity (i.e., the ratio of the reflected to the incident X-ray flux) is related to the laterally averaged electron density, $\rho(z)$, near a reflecting interface[21] through the equation

$$R(Q) = (4\pi r_e/QA_{uc})^2 \, | \int \rho(z)e^{iQz}dz \,|^2$$

$$= (4\pi r_e/QA_{uc})^2 \, | \Sigma_j f_j \exp(iQz_j) \exp[-(Q\sigma_j)^2] \,|^2 \quad (1)$$

where the momentum transfer, Q, is defined by the relation $Q = (4\pi/\lambda) \sin(\alpha)$ and is oriented in these measurements along the surface normal (i.e., specular) direction; α is the angle of incidence with respect to the surface plane; λ is the X-ray wavelength; and $r_e = 2.818 \times 10^{-5}$ Å is the classical electron radius. In the second expression, f_j, z_j, and σ_j are the atomic scattering factor, the position, and the vibrational amplitude of the jth atom in the crystal; the expression is summed over all atoms, j; and A_{uc} is the two-dimensional area of the unit cell ($A_{uc} = 48.4$ Å^2 and 100.7 Å^2 for the barite (001) and (210) surfaces). As is implicit in the form of eq 1, the data are analyzed in a fully atomistic perspective. Equation 1 can be rearranged to a more descriptive form as

$$R = (4\pi r_e/QA_{uc})^2 \, | F_{bulk-uc} \, F_{ctr} + F_{surf} + F_{water} \,|^2 \quad (2)$$

in which $F_{bulk-uc}$ represents the sum over atoms in a single bulk unit cell, F_{ctr} is an additional phase factor that represents a semi-infinite lattice,[22] F_{surf} is the sum over all atoms near the interface (e.g., including adsorbed molecules and substrate atoms in the top few unit cells that may be displaced), and F_{water} is the sum over atoms in the semi-infinite fluid water layer above the surface. We have assumed that the sulfate ions near the surface relax as rigid bodies. All symmetry-allowed structural relaxations, the presence of steps,[22] surface vacancies, and any layering in the water above the mineral surface are incorporated into this expression through suitable parametrizations, providing a realistic physical description of the barite−water interface. From the form of eq 2, it can be seen that the measured reflectivity of the barite−water interface is the result of interference between X-rays scattered from the bulk barite crystal, the barite−water interfacial region, and the water layer above the surface. Although the bulk structure is known a priori, the surface structure is not. The surface structure involves relatively few atoms (as compared with the bulk structure), so the greatest influence of the interfacial structure on the X-ray reflectivity is where the bulk contribution is minimal. It is therefore the modulation of the X-ray reflectivity between the bulk Bragg peaks that provides information on the barite−water interfacial structure.

The simple and direct relationship between reflectivity and $\rho(z)$, as described in eqs 1 and 2, makes it possible to quantitatively test and optimize models for the interface structure at the atomic scale[21] through least-squares fitting techniques. We use the χ^2 function as a measure of the quality of fit, where χ^2 approaches a value of ~ 1 when the fit is within the experimental error (i.e., when the average difference between data and calculation is comparable to the experimental uncertainty).[15] This formalism also provides a quantitative estimate for the uncertainty associated with the structural determination that is derived directly from the experimental data.[23] The error for each parameter is reported as the 2σ uncertainty, corresponding to a 95% confidence level.

An important feature of any scattering measurement is the associated resolution, L, that varies inversely with the data range and is estimated using the relation $L \sim 2\pi/Q_{max}$, where Q_{max} corresponds to the largest momentum transfer achieved in the measurement. The X-ray reflectivity measurements reported herein were performed to a momentum transfer of $Q_{max} \sim 6$ Å^{-1} resulting in a resolution of ~ 1 Å. This provides a simple estimate for the length scale over which the structure can be determined uniquely. The data are, however, sensitive to atomic displacements as small as ~ 0.05 Å.

The X-ray reflectivity measurements were performed at bending-magnet station 1-BM (SRI-CAT) of the Advanced Photon Source at Argonne National Laboratory.[24] The specular geometry of these measurements is shown schematically in Figure 2. A monochromatic X-ray beam having a wavelength of 0.775 Å (corresponding to a photon energy of 16 keV) is incident upon the surface at a small angle, α, and the incident and reflected photon fluxes are measured separately as a function of α. The photon energy was chosen with a sagitally focusing Si(111) monochromator, and the beam was vertically focused with a Pd-coated harmonic rejection mirror. A typical incident X-ray flux was $\sim 10^{10}$ photons/s through an aperture of 0.1 mm (vertical) by 1.6 mm (horizontal) placed just before the sample. The reflected flux at each momentum transfer, Q, is determined by performing a rocking-curve scan in which the angular position of the detector is fixed while the incident angle, α, is scanned through the specular reflection condition. By fitting
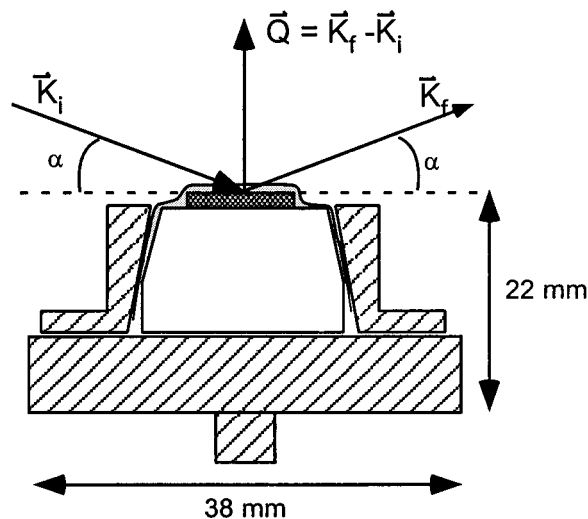
Figure 2. Schematic representation of the experimental geometry. The X-rays are incident upon the surface at a grazing angle, α, and specularly reflected corresponding to vector momentum transfer, $\mathbf{Q} = \mathbf{K}_f - \mathbf{K}_i$, where $|\mathbf{K}| = 2\pi/\lambda$ is the wave-vector of the X-ray photon and $|\mathbf{Q}| = (4\pi/\lambda) \sin(\alpha)$. Also shown is a schematic of the thin-film reflectivity cell used for the present experiments.

each rocking-curve scan to a suitably chosen peak-shape and a linear background, the integrated reflected flux and transverse shape of the specular rod (and associated uncertainties) are determined as a function of the momentum transfer. The uncertainties in these quantities are related to the counting statistics in the rocking curve data. We used a pseudo-Voigt line shape to fit the rocking-curve profiles.

Atomic Force Microscopy. Atomic force microscopy images were obtained using a Digital Instruments Nanoscope III

Multimode AFM operating in contact mode. A commercially available fluid cell was used, and the samples were imaged in deionized water. We used pyramidal Si_3N_4 tips attached to a V-shaped cantilever with a spring constant of 0.06 N/m. Further details about the AFM measurements can be found elsewhere.[2]

Sample Preparation. Single crystals of optically clear, natural barite were cleaved to expose either (001) or (210) surfaces (unit cell $a = 8.884$ Å, $b = 5.457$ Å, $c = 7.157$ Å, space group *Pbnm*).[25] Cleaved samples were approximately 50−100 mm^2 and 1−2 mm thick. For the X-ray reflectivity measurements, cleavage of barite in air was followed quickly (<1 min) by immersing the cleavage surface in deionized water at room temperature and mounting the crystal in the X-ray reflectivity cell. Experiments were performed in a static thin-film configuration as shown in Figure 2,[16] with a water layer having a typical thickness of ∼60 μm at the barite surface contained by an 8-μm Kapton film. Each data set was measured in less than 7 h. No apparent physical or chemical changes of the Kapton film resulted from irradiation.

3. Defect Structures at Barite−Water Interfaces

Surface defect structures on barite have been well-characterized by using a combination of atomic force microscopy and X-ray reflectivity. An in situ atomic force microscopy (AFM) image of a freshly cleaved barite (001) surface is shown in Figure 3. This image showing a scan area of 1.4 μm × 1.4 μm shows that the predominant defects are individual steps with a measured height of 7.2 Å. Except for these individual steps, the barite surface presents large featureless terrace regions indicative of a uniform, ideally terminated barite surface.

Representative rocking-curve scans of the barite−water interface are shown in Figure 4a at selected values of Q for the
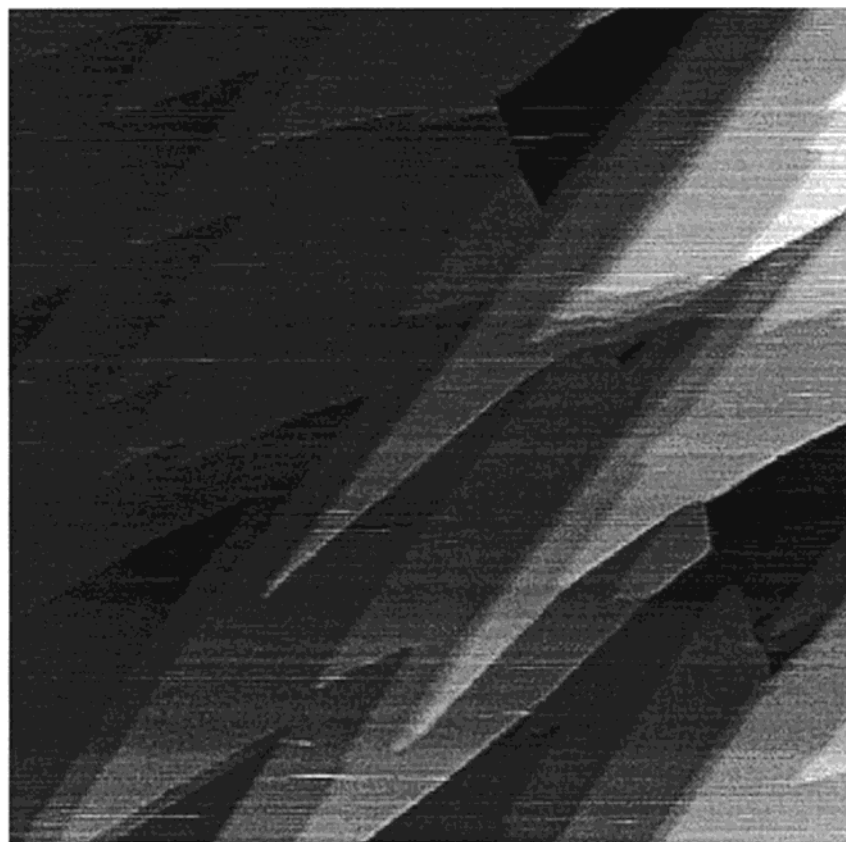
Figure 3. AFM image of freshly cleaved barite (001) surface (1.4 μm × 1.4 μm) in contact with water. The defects are predominantly unit-cell high steps (7.2 Å in height), or steps having integer numbers of unit cells. No roughness is observed in this image in the terrace areas.

Structure of Barite (001)− and (210)−Water Interfaces

J. Phys. Chem. B, Vol. 105, No. 34, 2001 **8115**
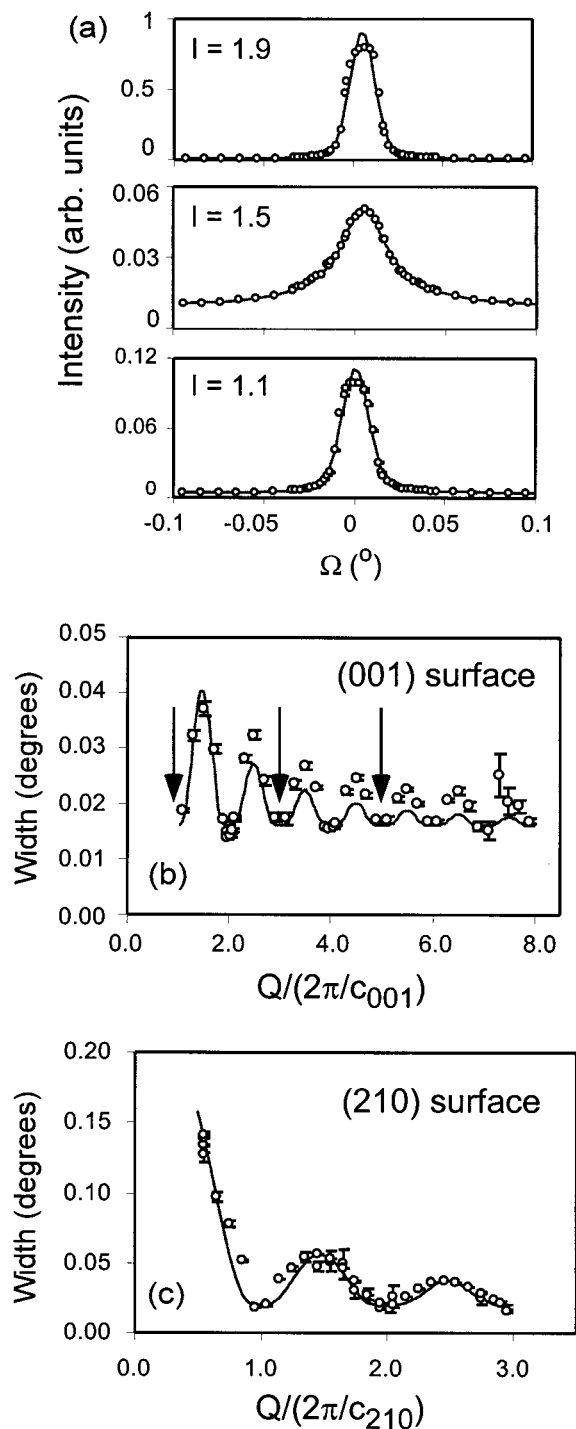
Figure 4. (a) Rocking-curve scans for the (001) surface are shown at selected values of l = $Q/(2\pi/c_{001})$ as a function of $\Omega = \theta - (2\theta_0)/2$, where $2\theta_0$ is the scattering angle for each scan. The rocking curves are well-described by a pseudo-Voigt line shape that changes from an approximately Lorentzian line shape at half-integer multiples of $2\pi/c_{001}$ to an approximately Gaussian line shape at integer multiples of $2\pi/c_{001}$. The width of the rocking curve also oscillates as a function of Q. The variation of the rocking-curve width as a function of Q for the (b) (001) and (c) (210) surfaces. Also shown are the predictions (solid lines) of the model described in the text. This model reveals that the steps are unit-cell high in both cases, and the mean lateral step−step spacing is ∼7300 Å and ∼2300 Å for the (001) and (210) surfaces, respectively. The vertical arrows in (b) show the location where broadening would be maximized for half-unit cell steps; the lack of any significant broadening beyond our resolution limit at these scattering conditions implies that there is a negligible density of half-unit cell high steps.

(001) surface. Also shown in Figures 4b and 4c are the rocking-curve widths plotted as a function of the momentum transfer, Q, for both the (001) and (210) surfaces. The data in Figure 4a clearly show that the rocking-curve scans for the (001) surface vary in both shape and width as a function of Q. While the rocking-curve scans are narrow with a Gaussian-like shape near $Q = 2\pi n/c_{hkl}$ when n is an integer and c_{hkl} is the unit-cell dimension in the surface normal direction ($c_{001} = 7.157$ Å, and $c_{210} = 3.44$ Å), they have a Lorentzian-like shape and are broader near half-integer values of n. Their widths oscillate as a function of Q from a maximum of ∼0.04° to a minimum of <0.02°. The minimum widths are a result of the finite angular resolution of the detector that was independently measured by scanning the detector slit (having a nominal 0.6 mm-wide aperture) through the direct beam (having a vertical cross section of 0.1 mm) resulting in a measured angular detector width of $\Delta(2\theta) = 0.038°$. Rocking-curve widths broader than $\Delta\theta = \Delta(2\theta)/2 = 0.019°$ result from the defect structure of the barite surface. A stronger variation in the rocking curve width was observed for the (210) surface (Figure 4c) with a maximum rocking curve width of 0.15° at small Q and resolution limited widths of ∼0.02° at successive minima.

A Lorentzian-like line shape indicates random defect distribution across the surface. The oscillation of the rocking-curve width as a function of Q is a direct result of constructive and destructive interference conditions that are alternately satisfied as the momentum transfer increases. The vertical extent of the defects, h, is revealed through the relation, $h = 2\pi/\delta Q$, where δQ is the characteristic period of the oscillations. The periods of oscillations in Figure 4, parts b and c, are $\delta Q = 2\pi/c_{hkl}$ for both surfaces implying that for each surface the predominant defects correspond to unit-cell-high steps, having h = 7.2 and 3.4 Å on the (001) and (210) surfaces, respectively. This conclusion is consistent with previous AFM studies[2,3] (Figure 3).

An estimate for the lateral domain size, $L_{//}$, can be derived from the rocking-curve width, $\Delta\theta$, measured at a momentum transfer, Q, through the relation $L_{//} \sim 2\pi/(Q \times \Delta\theta)$. From this relation we estimate domain sizes of ∼7400 Å at $Q = 1.5 \times (2\pi/c_{001})$ for the (001) surface, and ∼2800 Å at $Q = 0.5 \times (2\pi/c_{210})$ for the (210) surface (this estimate ignores the dependence of the derived domain size upon the rocking curve line shape; a more quantitative estimate is derived below). In each case, the domain size can be thought of as the mean step−step spacing. Larger values > 10 000 Å (corresponding to the narrowest rocking curve widths) are found at constructive interference conditions when scattering from neighboring terraces is in-phase, reflecting the surface domain size when the steps are ignored. These values are expressed as lower limits because the measurements are limited by the finite angular resolution of the detector (0.02°).

To provide a more quantitative description of the surface defect distributions, we use a model for randomly distributed surface defects.[26] With this model, the rocking-curve width and its variation with Q can be calculated from a few parameters that describe the probability of encountering a defect (i.e., a step), and the phase change in encountering that defect (for specular reflectivity, this phase change is due to the height difference across the step). Within this model, an approximate-Lorentzian line shape is reproduced.

Comparing this model to the measured rocking curve widths for the (210) surface (Figure 4c), we can explain our data with single unit-cell-high steps (randomly in either the up or down direction) having a mean step−step spacing of 2300 Å. This

model properly describes the periodicity of the oscillations for the (001) surface, confirming that the unit-cell-high step is the predominant defect averaged macroscopically over the (001) surface. However, the variation of the (001) rocking-curve width is not well described by this model assuming a defect spacing of 7300 Å (Figure 4b). The rate at which the rocking-curve width decreases with increasing Q is overestimated, implying a smaller-than-expected surface domain size at larger incident angle (and smaller X-ray footprint). We found by measuring separate spots on the sample surface that the domain size on this surface was inhomogeneous. The simplest explanation for these data is that the X-ray beam footprint at large values of Q (i.e., where the footprint was the smallest) was on an area with a relatively high step density, while at small values of Q the larger area of the X-ray beam footprint included areas having lower step densities. The mean step spacing determined by the rocking curve line shape analysis at small Q appears to be at least in qualitative agreement with the step distribution in the AFM image shown in Figure 3.

An interesting aspect of these data is that the step height observed for the (001) surface is, in fact, a unit-cell high, containing two separate $BaSO_4$ layers, as was previously observed by AFM.[2,3] The (001) surface is formed by alternating $BaSO_4$ layers (which we refer to as A and A′ layers) that are symmetry-related though a 2_1 screw axis (Figure 1a).[25] Consequently, there are no structural or chemical differences between surfaces terminated with the A and A′ layers, and there can be no thermodynamic driving force for this observation (i.e., differences in surface energies, or the number of broken bonds during cleavage). The absence of half-unit cell high steps can be noted from Figure 4b by the lack of any additional broadening at $Q = 2\pi n/c_{hkl}$ with $n = 1, 3, 5...$ (shown in Figure 4b as vertical arrows) where the sensitivity of the rocking curve width to half-unit cell high steps is maximized. Because there is no evidence for any broadening beyond experimental resolution at these scattering conditions, we conclude that unit-cell high steps are not simply typical defects, but instead are the predominant defects averaged over macroscopic surface regions, at least for this sample and all other samples that we have studied. The small finite lateral spatial resolution in our measurement (~ 1 μm), compared with the ~ 1 to 5 mm^2 areas covered by the X-ray beam footprint, does not change this conclusion; the interference responsible for the modulation in rocking curve width is observed in each micrometer-wide region associated with the X-ray coherence length. Since there is no evidence for steps with heights other than unit-cell high, we conclude that one of the two possible surface terminations is present over most of the barite surface.

To understand this, we note that the A−A′ interface has a directional anisotropy that is opposite to that of the A′−A interface due to the screw axis (Figure 1). While the screw axis is not expressed in the location of the Ba ions, the topmost $BaSO_4$ layer exposes sulfate ions that are tilted toward the [100] or [−100] direction for the A−A′ and A′-A interfaces, respectively, as drawn in Figure 1. This directional anisotropy is expressed along the [100] direction, but not in the orthogonal [010] direction. Based upon these considerations, our observation of a preference for unit-cell high steps leads to the following implications: (1) The dynamical cleavage process exhibits a microscopic preference for alignment, either with or against the orientation of the interfacial handedness. (2) The barite (001) cleavage surface should exhibit a net directional anisotropy even when averaged over macroscopic areas, and the direction of the surface anisotropy (i.e., either [001] or [00-1]) should be
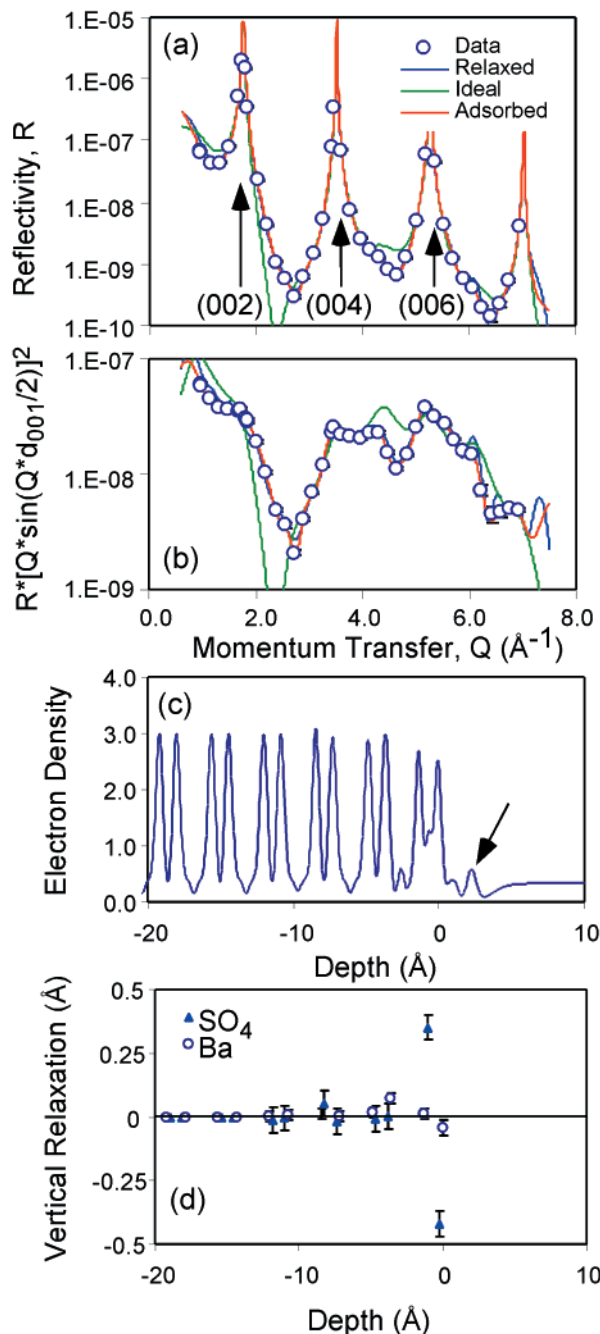
correlated with the cleavage direction. (3) While no attempt was made to orient the cleavage direction to any particular crystallographic direction in the present study, it is conceivable that cleavage along [010] would result in a surface with no net directional anisotropy. Therefore it may be possible to control both the magnitude and direction of the macroscopically averaged directional anisotropy with the cleavage direction.

A macroscopically controlled surface directional anisotropy might be useful in a range of applications, e.g., such as crystal growth or alignment of the molecular orientation of liquid crystal films, and should be a general characteristic of cleavage surfaces orthogonal to a screw axis. This phenomena is similar to, but more subtle than, recent observations on the cleavage of potassium bichromate (having an A−B stacking). The termination of the potassium bichromate (001) surface upon cleavage was controlled by suitable choice of cleavage direction, resulting in an all-A or all-B termination.[27] An important difference here is that the A and A′ surfaces created during cleavage of barite (001) are identical, while the A and B terminations created by cleaving potassium bichromate are not related by any symmetry. However, the observation of a dynamical preference for a particular cleavage plane in both cases implies a deviation from the classic theory of Griffith[28] in which cleavage is assumed to be a succession of reversible thermodynamically controlled steps.

4. Atomic Structure of Barite−Water Interfaces

4.1. The Barite (001) Surface. The variation of the X-ray reflectivity, R, as a function of the momentum transfer, Q, of the barite(001)−water interface is shown in Figure 5. The data follow the expected form of a crystal truncation rod (CTR)[22] in which the reflectivity, R, is approximately unity at bulk Bragg peaks [notated as (002), (004), (006), etc., in Figure 5], but is as low as $\sim 10^{-10}$ between the bulk Bragg peaks (here the reflectivity is shown only for $R < 10^{-5}$). The absence of odd-order bulk Bragg reflections is due to the 2_1 screw-axis symmetry along [001], and reveals that the periodicity of the laterally averaged electron density along the [001] direction is one-half the unit cell height, $c/2 = 3.58$ Å. By analogy with the crystallography of a three-dimensional crystal, where the Bragg peak intensities provide a direct measure of the bulk crystalline structure, it is the continuous variation of the weak reflectivity between the barite Bragg peaks that provides sensitivity to the structure and termination of the barite−water interface.

A set of model reflectivity calculations is shown in Figure 5. The green curve is a prediction of the specular reflectivity for an ideally truncated barite (001) surface with no structural relaxation in the near-surface region, with the water being modeled by an error function profile indicating a featureless structure. The only aspects of the structure that were optimized in this model were the surface roughness factor, β, and the position of the semi-infinite water layer above the barite surface, neither of which can be known a priori. This model provides a poor representation of the data, and has a quality of fit of $\chi^2 = 208$. Inclusion of symmetry-allowed substrate relaxation (including vertical motions of both Ba and SO_4 ions, as well as rotation of the SO_4 ions) in the top barite unit cell improves the quality of fit to $\chi^2 = 60$. Additional substrate relaxation in the second unit cell below the surface improves the quality of fit further to $\chi^2 = 25$. While this fit (blue line, Figure 5) is substantially improved and provides a fairly good description of the data, it does not explain all the fine structure in the data, as can be seen when the data are multiplied by $[Q \sin(Qc_{001}/$

Structure of Barite (001)− and (210)−Water Interfaces

J. Phys. Chem. B, Vol. 105, No. 34, 2001 **8117**

Figure 5. (a) Comparison of the experimental reflectivity of the barite (001)−water interface to model calculations including an ideally truncated surface, a surface that has been relaxed with symmetry allowed displacements, and a surface with adsorbed water molecules. (b) The same data and calculations as shown in (a) shown normalized to the form of the crystal truncation rod, $R_{norm} = R \times [Q \times \sin(Q \times d_{001}/2)]^2$. (c) The electron density profile for the best-fit structure is shown. Note that this profile includes broadening that is representative of the finite resolution of the experimental data. The arrow highlights the electron density due to adsorbed water molecules. (d) Derived vertical relaxations at the barite (001) interface for the Ba and SO$_4$ groups as a function of the vertical height of each atom.

2)]^2, to remove the strong variation of the CTR intensity as a function of Q due to the presence of the bulk barite Bragg peaks (Figure 5b). We finally include the possibility that water near the barite surface may be structured, by allowing for a layer of adsorbed water molecules. This results in a quantitative fit to the data with $\chi^2 = 0.7$ (red line in Figure 5). This shows that the inclusion of adsorbed water molecules is significant with respect to the uncertainties in the experimental data, although

the absolute changes in the calculated reflectivity are small as plotted in Figure 5. Since $\chi^2 = 1$ corresponds to a fit that is within the statistical error of the experimental data, this implies that there are no additional structural features present in these data.

The electron density profile corresponding to the best-fit structure is shown in Figure 5c. The electron density is plotted to simulate the finite resolution of the experiment, in which the effective electron density of each atom, ρ_{eff}, is plotted as a Gaussian function with an effective "vibrational amplitude" due to the finite resolution of u_{eff}, or

$$\rho_{eff}(z) = Z/[(2\pi)^{0.5} \, u_{eff}] \exp[-0.5 \times ((z - z_0)/u_{eff})^2] \quad (3)$$

where z_0 is the position of a particular atom having an atomic charge of Z. For generality, the net effective vibrational amplitude, $u_{eff}(j)$, for each atom, j, is determined by adding the resolution width, u_{res}, and the true vibrational amplitude, σ_j, in quadrature, or $u_{eff}(j) = (u_{res}^2 + \sigma_j^2)^{1/2}$, where u_{res} is assigned the value, $u_{res} = 1.1/Q_{max}$ and Q_{max} is the maximum momentum transfer in the measurement. To motivate this choice of u_{res}, we note that the Patterson function, $P(x)$, is the density−density correlation function and can separately be derived from experimental data. It can be written as

$$P(x) = \int \rho_{eff}(x) \, \rho_{eff}(x + X) \, dX = \int I(Q) \cos(Qx) \, dQ \quad (4)$$

where we define $\rho_{eff}(x)$ to be the effective electron density of the material as seen at the finite resolution of the measurement, and $I(Q)$ is the measured reflectivity. In the second expression of eq 4, the Patterson function will be expressed by a series of terms that have the form of $\sin[Q_{max}(x - x_0)]/(x - x_0)$, where the location of each term, x_0, is determined by the details of the structure but the width of each term is determined only by Q_{max}. Assuming that the effective electron density of a particular atom can be expressed by a Gaussian function with a width u_{res} as written in eq 3, $P(x)$ will be a sum of Gaussian functions having widths of $\sqrt{2}u_{res}$. The numerical value of $u_{res} \approx 1.1/Q_{max}$ provides good correspondence between these two expressions in eq 4 when $Q_{max} > 2$ Å^{-1}.

The derived Ba and SO$_4$ relaxations in the near surface region are plotted in Figure 5d. These results show that Ba ions are displaced from their bulk lattice locations by ∼0.07 Å near the surface, while the outermost SO$_4$ ions show a larger displacement of ∼0.4 Å. We also find significant rotations of the near-surface SO$_4$ ions, with derived tilt angles with respect to the surface normal direction of 0, 8, 19, and 0° (with a statistical error of 4°) starting with the outermost SO$_4$ ion. Because these results are largely insensitive to the tilt direction, it is difficult to independently assess if these rotations are uniquely determined in the absence of nonspecular reflectivity data (which probes the lateral surface structure). In all cases, these structural distortions decay rapidly into the crystal. The SO$_4$ displacements appear to be significant ∼3 Å into the barite surface (i.e., within the outermost BaSO$_4$ bilayer). Also included in this best-fit structure is the surface roughness parameter,[22] $\beta = 0.028 \pm 0.01$, corresponding to a surface roughness (due entirely to steps) of 1.1 ± 0.2 Å rms roughness averaged over the ∼1 μm coherence length of the incident X-ray beam. The best-fit model includes an adsorbed water layer at a height of 2.35 ± 0.13 Å above the outermost Ba ion, having 2.7 ± 0.1 water molecules per barite(001) surface unit mesh (the unit mesh area is 48.4 Å^2). These measurements are insensitive to the presence of protons, therefore the molecular species of the water (e.g.,

hydroxyl or hydronium) cannot be uniquely identified from these data; we refer to these simply as water molecules for convenience.

The measured water coverage is significantly smaller than that expected for a close-packed water layer (~1 molecule/10 Å^2 surface area, or 4.8 water molecules per unit mesh) as would be expected if the barite surface acted as a chemically inert "hard wall". Instead, we consider that there are 4 Ba−O bonds broken at the (001) surface per unit mesh due to cleavage (3 to the outer Ba ion, 1 to the inner). Of these, two broken bonds from the outer Ba to its nearest neighbor oxygens have a Ba−O height difference of 2.4 Å, the third has a Ba−O height difference of 1.9 Å, and the broken bond associated with the second layer Ba ion has a Ba−O height difference of 1.5 Å with respect to the upper Ba ion (these height differences are derived from the unrelaxed bulk barite structure). The observed height for the adsorbed water layer is similar to average nominal Ba−O height (2.2 Å) associated with the upper Ba ion's three broken bonds, and the number of adsorbed water species are moderately consistent with this as well (2.7 ± 0.1 vs 3.0 Å). This suggests that the adsorbed water molecules saturate the broken bonds of the surface Ba ions, in analogy to that observed previously for Ca ions at the calcite−water interface.[12]

Including additional adsorbed water to saturate the single broken Ba−O bond associated with the inner Ba ion did not improve the fit (as expected since the quality of fit was ~1). Such models also resulted in a high degree of covariance between the parameters associated with the adsorbed water structure, further implying that these data cannot uniquely determine any further detail of the adsorbed water structure. Nonspecular X-ray reflectivity data will be needed to provide additional information on both the lateral and vertical structure near the barite−water interface.

4.2. The Barite (210) Surface. X-ray reflectivity data are shown for the barite (210)−water interface in Figure 6. These data show a typical CTR shape with the strong (210), (420), and (640) Bragg reflections and the much weaker reflectivity between Bragg peaks due to scattering from the barite−water interface. As shown in Figure 1b, the (210) surface consists of alternating 3.6 Å-wide nano-terrace areas along the [001] direction that differ in height by $\delta z = 0.8$ Å. To model the adsorbed water structure and the semi-infinite bulk water above the barite surface, we have assumed simply that the semi-infinite water layer follows the surface contours conformally, and that the adsorbed water species is located at the same height with respect to the Ba ions in each nano-terrace. This modest simplification allows us to model the adsorbed water and semi-infinite liquid water structures each with a single water term corresponding to that above an atomically flat surface by using an additional phase factor, $[1 + \exp(iQ\,\delta z)]$. δz was held fixed at 0.8 Å in the optimization process.

As was the case for the (001) surface, an ideally terminated (210) surface without any structural relaxation near the interface provides a poor description of the data with a quality of fit of $\chi^2 = 51.8$, and the inclusion of near-surface relaxation improves this quality of fit to $\chi^2 = 4.1$. The inclusion of adsorbed water species improves the quality of fit to 1.9. This difference, although not as dramatic as that found upon including adsorbed water species on the (001) surface, is significant. It represents a 0.5σ reduction in the quality of fit per data point, or a total quality of fit improvement of 16σ.

A density profile corresponding to the best-fit (210) model is shown in Figure 6c. This model includes relaxations in the top two layers (each containing two terrace levels, as shown in
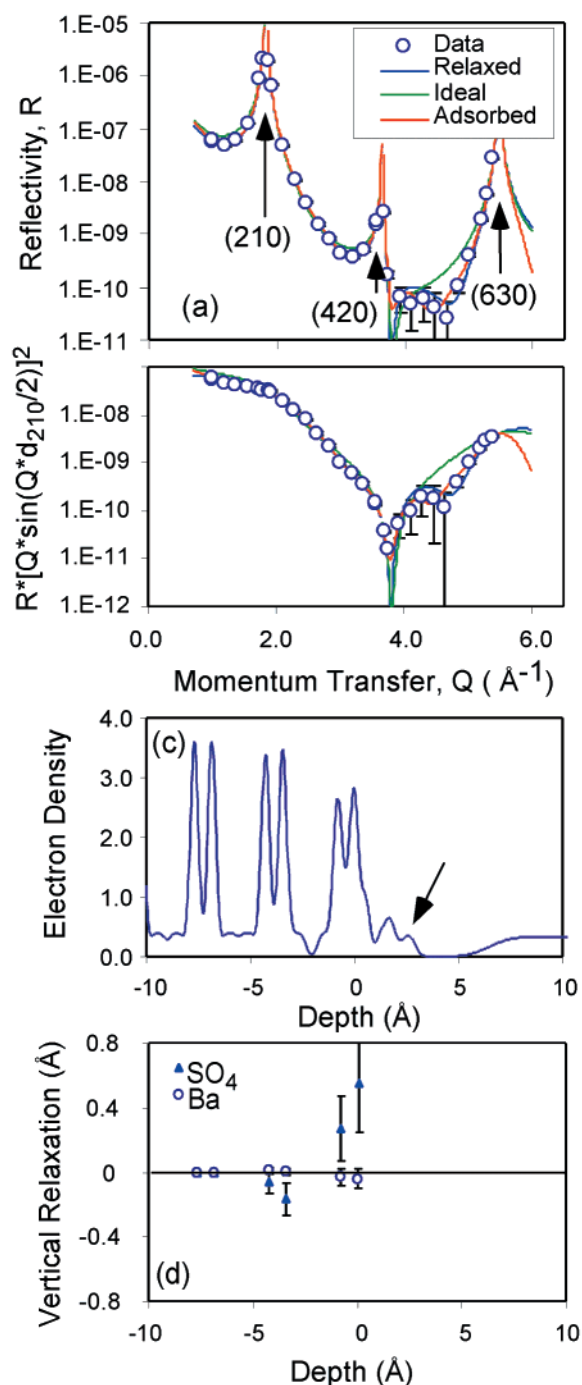
Figure 6. (a) Comparison of the experimental reflectivity of the barite (210)−water interface to model calculations including an ideally truncated surface, a surface that has been relaxed with symmetry allowed displacements, and a surface with adsorbed water molecules. (b) the same data and calculations shown normalized to the form of the crystal truncation rod, $R_{norm} = R \times [Q \times \sin(Q \times d_{210}/2)]^2$. (c) The density profile for the best-fit structure is shown. As in Figure 5, the plotted profile includes broadening due to the finite resolution of the measurement. The arrow highlights the electron density profile due to adsorbed water. (d) Derived vertical relaxations at the barite (210) interface for the Ba and SO$_4$ groups as a function of the vertical height of each atom.

Figure 1), and an adsorbed water species. The adsorbed water species is found to have 3.2 ± 2.5 water molecules per unit cell on both the upper and lower terraces, at a height of 2.6 ± 0.15 Å above the Ba ion of the respective terrace. For comparison, there are 8 broken Ba−O bonds per unit cell (4 above each nano-terrace) at heights ranging from 2.4 to 2.6 Å

Structure of Barite (001)− and (210)−Water Interfaces

J. Phys. Chem. B, Vol. 105, No. 34, 2001 **8119**

for the ideal bulk unit cell. So both the number and height of these adsorbed water species appear to be reasonable, although the adsorbed water coverage is relatively imprecise. The relaxations (Figure 6d) of the surface Ba ions are comparable to the size of the derived errors, although the outermost SO_4 ions are found to relax outwardly by ∼0.4 Å, and a smaller inward contraction is observed in the second $BaSO_4$ bilayer.

5. Discussion and Conclusions

The present results provide a fundamental understanding of the defect and crystal structures at the barite−water interface. The results show that the typical defects found at the (001) and (210) surfaces are unit-cell high steps that are randomly distributed across the surface with mean lateral spacings of ∼7300 and 2300 Å, respectively. In the case of the (001) surface, these steps consist of two $BaSO_4$ planes related by a 2_1 screw axis resulting in a net directional anisotropy of the barite (001) cleavage surface. We speculate that this double-step may be due to a dynamical effect during cleavage.

The barite (001)− and (210)−water interfaces both exhibit substantial structural relaxations (∼0.4 Å) of the outermost sulfate ions. Smaller but significant relaxations are also observed for the second layer sulfate ions within the outermost $BaSO_4$ unit cell. Smaller (∼0.07 Å) displacements were also observed for the near-surface Ba ions, and appear to decay in a similar fashion into the barite crystal.

An important aspect of the derived barite−water interface structure is the adsorption of water molecules whose positions and coverage are consistent with the interpretation that water molecules saturate the Ba−O bonds broken during cleavage. No additional structure is observed for the fluid water adjacent to the barite surfaces. We can compare these results to previous studies of water structure near solid−liquid interfaces. While there are four distinct Ba−O distances (along the surface normal direction) associated with broken bonds on both the (001) and (210) surfaces, there is only a single Ca−O height associated with broken bonds on the calcite (104) surface. Despite the higher structural heterogeneity of barite surfaces, we find that the location and number of adsorbed water molecules for both barite and calcite surfaces are consistent with the saturation of broken metal−oxygen bonds.[12] In each of these cases, the lateral two-dimensional densities of the adsorbed water layers [0.05 $H_2O/Å^2$ for calcite,[12] 0.056 $H_2O/Å^2$ for barite (001), and 0.06 $H_2O/Å^2$ for barite (210)] were found to be substantially smaller than that of a closed-packed water layer ($\rho_{2d} \sim \rho_{3d}^{2/3} \sim 0.10$ H_2O molecule/$Å^2$). This suggests the relatively simple picture that water acts to saturate broken bonds at ionic mineral surfaces. This picture has been recently corroborated by molecular dynamics (MD) simulations[29] in the case of the calcite−water interface. This implies that the adsorbed water structure can be understood in the context of the general characteristics of water−cation interactions that were included in the MD simulations. In contrast to these results, highly structured water layers found at electrified Ag(111) and Au(111) metal interfaces[18,19] have densities that are either equal to or greater than the closed-packed densities associated with a densely packed water monolayer. No significant structuring was found in either case in the absence of an applied field, suggesting that these structures are instead primarily associated with the perturbation of the near-surface water due to the applied electric fields. Recent results at the electrified RuO_2(110) interface find a result that is intermediate between these two regimes and is also sensitive to the applied potential.[20]

References and Notes

(1) Benton, W. J.; Collins, I. R.; Cooper, S. D.; Grimsey, I. M.; Parkinson, G. M.; Rodger, S. A. *Faraday Discuss.* **1993**, *95*, 281−297.

(2) Bosbach, D.; Hall, C.; Putnis, A.; *Chem. Geol.* **1998**, *151*, 143−160.

(3) Pina, C. M.; Becker, U.; Risthaus, P.; Bosbach, D.; Putnis, A. *Nature* **1998**, *395*, 483−486.

(4) Rohl, A. L.; Gay, D. H.; Davey, R. J.; Catlow, C. R. A. *J. Am. Chem. Soc.* **1996**, *118*, 624.

(5) Higgins, S. R.; Bosbach, D.; Eggleston, C. M.; Knauss, K. G. *J. Phys. Chem. B* **2000**, *104*, 6978−6982.

(6) Putnis, A.; Junta-Rosso, J. L.; Hochella, M. F., Jr. *Geochim. Cosmochim. Acta* **1995**, *59*, 4623−4632.

(7) Wang, K.-S.; Resch, R.; Dunn, K.; Shuler, P.; Tang, Y.; Koel, B. E.; Yen, T.-F. *Langmuir* **2000**, *16*, 649−655.

(8) Davey, R. J.; Black, S. N.; Bromley, L. A.; Cottier, D.; Dobbs, B.; Rout, J. E. *Nature* **1991**, *353*, 549−550.

(9) Black, S. N.; Bromley, L. A.; Cottier, D.; Davey, R. J.; Dobbs, B.; Rout, J. E. *J. Chem. Soc., Faraday Trans.* **1991**, *87*, 3409−3414.

(10) Hartman, J.; Strom, C. S. *J. Cryst. Growth* **1989**, *97*, 502−512.

(11) Allan, N. L.; Rohl, A. L.; Gay, D. H.; Catlow, C. R. A.; Davey, R. J.; Mackrodt, W. C. *Faraday Discuss.* **1993**, *95*, 273−280.

(12) Fenter, P.; Geissbuhler, P.; Di Masi, E.; Srajer, G.; Sorensen, L. B.; Sturchio, N. C. *Geochim. Cosmochim. Acta* **2000** *64*, 1221−1228.

(13) Chiarello, R. P.; Sturchio, N. C. *Geochim. Cosmochim. Acta* **1995**, *59*, 4557−4561.

(14) Chiarello, R. P.; Wogelius, R. A.; Sturchio, N. C. *Geochim. Cosmochim. Acta* **1993**, *57*, 4103−4110.

(15) Fenter, P.; Teng, H.; Geissbuhler, P.; Hanchar, J. M.; Nagy, K. L.; Sturchio, N. C. *Geochim. Cosmochim. Acta* **2000**, *64*, 3663−3673.

(16) Fenter, P.; Sturchio, N. C. *Geochim. Cosmochim. Acta* **1999**, *63*, 3145−3152.

(17) DeVries, S. A.; Goedtkindt, P.; Bennett, S. L.; Huisman, W. J.; Zwanenburg, M. J.; Smilgies, D.-M.; De Yoreo, J. J.; van Enckevort, W. J. P.; Bennema, P.; Vlieg, E. *Phys. Rev. Lett.* **1998**, *80*, 2229−2232.

(18) Toney, M. F.; Howard, J. N.; Richer, J.; Borges, G. L.; Gordon, J. G.; Melroy, O. R.; Wiesler, D. G.; Yee, D.; Sorensen. L. B. *Nature* **1994**, *368*, 444−446.

(19) Wang, J.; Ocko, B. M.; Davenport, A. J.; Isaacs, H. S. *Phys. Rev. B* **1992**, *46*, 10321−10338.

(20) Chu, Y. S.; Lister, T. E.; Cullen, W. G.; You, H.; Nagy, Z. *Phys. Rev. Lett.* **2001**, *86*, 3364−3367.

(21) Feidenhans'l, R. *Surf. Sci. Rep.* **1989**, *10*, 105−188.

(22) Robinson, I. M. *Phys. Rev. B* **1986**, *33*, 3830−3836.

(23) Bevington, P. R. *Data Reduction and Error Analysis for the Physical Sciences*, 1969; MacGraw-Hill Book Company: New York, 1969.

(24) Lang, J. C.; Srajer, G.; Wang, J.; Lee, P. L. *Rev. Sci. Instrum.* **1999**, *70*, 4457−4462.

(25) Miyake, M.; Minato, I.; Morikawa, H.; Iwai, S.-I. *Am. Mineral.* **1978**, *63*, 506−510.

(26) Lu, T.-M.; Lagally, M. G. *Surf. Sci.* **1982**, *120*, 47−66.

(27) Plomp, M.; van Enckevort, W. J. P.; Vlieg, E. *Phys. Rev. Lett.* **2001** *86*, 5070−5072.

(28) Griffith, A. A.; Philos. Trans. R. Soc. London **1921**, *A221*, 163.

(29) Wright, K.; Cygan, R. T.; Slater, B. *Phys. Chem. Chem. Phys.* **2001** *3*, 839−844.